mathematics

MDPI

Article

Impact of Astrocytic Coverage of Synapses on the Short-Term Memory of a Computational Neuron-Astrocyte Network

Zonglun Li [1,2], Yuliya Tsybina [3,4], Susanna Gordleeva [3,5] and Alexey Zaikin [1,2,3,4,*]

1 Department of Mathematics, University College London, London WC1E 6BT, UK
2 Institute for Women's Health, University College London, London WC1E 6BT, UK
3 Department of Neurotechnology, Lobachevsky State University of Nizhny Novgorod, 603022 Nizhny Novgorod, Russia
4 World-Class Research Center "Digital Biodesign and Personalized Healthcare", Sechenov University, 119991 Moscow, Russia
5 Neuroscience Research Institute, Samara State Medical University, 443099 Samara, Russia
* Correspondence: alexey.zaikin@ucl.ac.uk

Abstract: Working memory refers to the capability of the nervous system to selectively retain short-term memories in an active state. The long-standing viewpoint is that neurons play an indispensable role and working memory is encoded by synaptic plasticity. Furthermore, some recent studies have shown that calcium signaling assists the memory processes and the working memory might be affected by the astrocyte density. Over the last few decades, growing evidence has also revealed that astrocytes exhibit diverse coverage of synapses which are considered to participate in neuronal activities. However, very little effort has yet been made to attempt to shed light on the potential correlations between these observations. Hence, in this article, we leverage a computational neuron–astrocyte model to study the short-term memory performance subject to various astrocytic coverage and we demonstrate that the short-term memory is susceptible to this factor. Our model may also provide plausible hypotheses for the various sizes of calcium events as they are reckoned to be correlated with the astrocytic coverage.

Keywords: neuron; astrocyte; network; short-term memory; spatial frequency; computational biology

MSC: 92B20

Citation: Li, Z.; Tsybina, Y.; Gordleeva, S.; Zaikin, A. Impact of Astrocytic Coverage of Synapses on the Short-Term Memory of a Computational Neuron-Astrocyte Network. *Mathematics* **2022**, *10*, 3275. https://doi.org/10.3390/math10183275

Academic Editor: Ichiro Tsuda

Received: 5 August 2022
Accepted: 6 September 2022
Published: 9 September 2022

1. Introduction

Over the past few decades, the dynamics of neuronal networks have been widely studied [1–7] and increasing effort has been devoted to understanding the roles played by a type of glial cells, astrocytes [8–13]. Traditionally, astrocytes have been reckoned as auxiliary cells to neurons and it has now become evident that astrocytes can not only support the structure of the nervous system, but also modulate synaptic transmission [14–18]. Neuron–astrocyte coupling plays an indispensable role in the functioning of neuronal networks via bidirectional communication under the notion 'tripartite synapse' [19–23]. It is found that astrocytes can sense the synaptic activities by the uptake of neurotransmitters released from the synaptic cleft and provide feedback to pre- and post-synaptic neurons via gliotransmitter release caused by the temporary elevation of intracellular calcium concentration which normally lasts seconds to minutes [24–28]. All these findings in molecular biology pave the way for a better understanding of the information processing in neuron–astrocyte circuits and the formation of cognitive functions. Very recently, mathematical and computational approaches have been used to investigate the contribution of astrocytes to the organisation of spatial and temporal synchronization in neural networks [29–32], formation of short-term memory [33–38] and generation of integrated information in neuronal ensembles [39–42], which takes a step further to the understanding of the intelligence arising from the nervous system.

Nowadays, a widely accepted fact is that astrocytes play an active role in various types of memory and the memory improvement may be related to the change in the astrocyte density [43–47]. Working memory is the ability of an entity to retain limited information in a readily accessible form and provides an interface between memory and cognition [48–50]. Some biological evidence has already raised the possibility that astrocytes could be highly involved in working memory [51–54] and it has been well known that the astrocytic coverage of synapses is a highly dynamic process that alters throughout lifetime [55–57]. Therefore, it is natural to hypothesize that there exists a potential correlation between the working memory and the astrocytic coverage (or astrocyte density) but very little effort has been made so far. In this work, the astrocytic coverage is equivalent to the astrocyte density and it will become clear when we introduce our model. Furthermore, some studies have also revealed that the attenuation of calcium events correlates with the reduction of astrocytic coverage of asymmetric synapses in the hippocampal CA1 region in mice and that the size of the calcium events within astrocytes follows the power law [58–61]. Hence, this line of research may also help explain the cause of various sizes of calcium events.

Lately, an in silico neuron–astrocyte network model has been employed to manifest that astrocytes indeed assist the formation of short-term memory and mediate analogous memory [34–38]. It provides a quantitative score to measure the recall accuracy as a result of the short-term memory. In this work, we leverage this computational model and study the impact of varying astrocytic coverage areas of synapses on the short-term memory performance. Unlike in the original article [35], here, we focus on the performance of the single-item task so as to ensure that the real pattern remains unchanged throughout the experiment. We also introduced a low-pass filter to the input image in order to alter the spatial frequencies. In particular, it is of great interest to learn how the change in the number of spatial frequency components will impact the short-term memory and how the relation is affected by the astrocytic coverage. The input image is also subject to different levels of the salt-and-pepper noise to make our evaluation more comprehensive. We demonstrate that the short-term memory performance is significantly affected by the astrocytic coverage. Additionally, we also underlie some other observations that may interest biologists.

2. Models and Methods

Our work employed the neuron–astrocyte network developed in [35] and an illustrative diagram for the architecture is shown in Figure 1. From left to right are the input image, neuronal network and astrocytic network, respectively. The neuronal network is of dimension $W \times W$ and the astrocytic network is of dimension $M \times M$. All neurons are excitatory and each astrocyte from the astrocytic network regulates an $l \times l$ neuronal square from the neuronal network. The connections in the neuronal network will be defined later and the astrocytes in the astrocytic layer are connected to their nearest neighbours vertically and horizontally. The input digital image is converted into electric current and is applied to the neuronal network in that one image pixel corresponds to exactly one neuron. The values used for the parameters introduced in Sections 2.1–2.3 are listed in [35], unless otherwise specified. The novel methodology used to study the impact of astrocytic coverage on short-term memory is introduced in Sections 2.4–2.6.

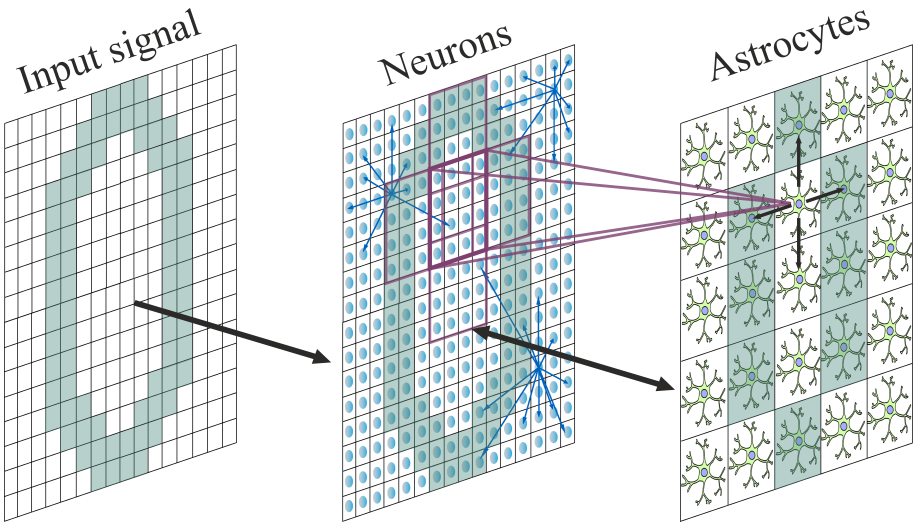

Figure 1. An illustrative diagram for the neuron–astrocyte network.

2.1. Neuronal Network

Considering we simulated a relatively large network, we used the Izhikevich model to characterize the dynamics of neurons as it demonstrates computational efficiency while maintaining the biological plausibility of the canonical Hodgkin–Huxley model [62]:

$$\begin{cases} \dfrac{dV^{(i,j)}}{dt} = 0.04V^{(i,j)^2} + 5V^{(i,j)} - U^{(i,j)} + 140 + I_{app}^{(i,j)} + I_{syn}^{(i,j)} \\ \dfrac{dU^{(i,j)}}{dt} = a(bV^{(i,j)} - U^{(i,j)}) \end{cases} \tag{1}$$

where V denotes the membrane potential of a particular neuron and U represents the membrane recovery variable, with post-spike resetting: if $V^{(i,j)} \geq 30$ mV, then

$$\begin{cases} V^{(i,j)} = c \\ U^{(i,j)} = U^{(i,j)} + d \end{cases} \tag{2}$$

The superscript (i, j) denotes the positional index of the neuron. I_{app} represents the applied input current converted from the digital image and I_{syn} represents the net current receiving from all presynaptic neurons which takes the form (generalized from [63,64]):

$$I_{syn}^{(i,j)} = \sum_k \frac{g_{syn}^{(i,j)}(E_{syn} - V^{(i,j)})}{1 + \exp\left(\frac{-V_{pre}^k}{k_{syn}}\right)} \tag{3}$$

where the summation is over all presynaptic neurons. The synaptic weight is dictated by $g_{syn}^{(i,j)} = \eta + \nu^{(i,j)}$ where η reflects the baseline weight and $\nu^{(i,j)}$ describes the impact of astrocytic calcium events which will be defined later. E_{syn} denotes the reversal potential for excitatory synapses and V_{pre}^k denotes the membrane potential of the neuron k. For clarity, we need to point out that the short-term synaptic plasticity is not considered in our model. By convention, we use $a = 0.1, b = 0.2, c = -65, d = 2$.

In this work, we fixed the number of out-connections per neuron as N_{out} in that each presynaptic neuron interacts with N_{out} postsynaptic neurons. The connections are

established according to an exponential distribution with R being the distance between each pair of neurons:

$$f(R) = \begin{cases} \frac{1}{\lambda} \exp(-R/\lambda) & R \geq 0 \\ 0 & R < 0 \end{cases} \tag{4}$$

2.2. Action Potential-Induced Elevation of Glutamate and IP_3

For each presynaptic neuron, the amount of glutamate, a type of neurotransmitter released into the synaptic cleft is dictated by the spiking events of the neuron [65]:

$$\frac{dG^{(i,j)}}{dt} = -\alpha_{glu} G^{(i,j)} + k_{glu} \Theta(V^{(i,j)} - 30) \tag{5}$$

where Θ denotes the Heaviside function.

IP_3 is a ligand and is produced in response to the external stimuli such as neurotransmitters [66]. It regulates many pathways including the release of Ca^{2+} from Endoplasmic Reticulum (ER) into cytoplasm [67] which will be described in due course. The dynamics of the intracellular concentration of the molecule IP_3 within each astrocyte is described by

$$\frac{dIP_3^{(m,n)}}{dt} = \frac{IP_3^{\star} - IP_3^{(m,n)}}{\tau_{IP_3}} + J_{PLC_\delta}^{(m,n)} + J_{glu}^{(m,n)} + diff_{IP_3}^{(m,n)} \tag{6}$$

Here, $IP_3^{\star}$ denotes the steady state of the intracellular IP_3 concentration and J_{PLC_δ} encapsulates the IP_3 produced by phospholipase $C\delta$ which takes the form

$$J_{PLC_\delta} = \frac{v_4(Ca + (1-\alpha)k_4)}{Ca + k_4} \tag{7}$$

where Ca denotes the Ca^{2+} concentration in the astrocytic cytoplasm. We use $diff_{IP_3}$ to represent the diffusion of IP_3 via gap junctions between adjacent astrocytes and is given by

$$diff_{IP_3} = d_{IP_3}(\Delta IP_3) \tag{8}$$

where ΔIP_3 denotes the discrete Laplace operator reflecting the diffusion as a result of Ca^{2+} exchange with neighbouring astrocytes. The production of IP_3 stimulated by glutamate via metabotropic glutamate receptors (mGluRs) and phospholipase $C\beta$ is characterized by

$$J_{glu} = \begin{cases} A_{glu} & t_0 < t \leq t_0 + t_{glu} \\ 0 & \text{otherwise} \end{cases} \tag{9}$$

where t_{glu} denotes the duration that persists since time t_0, when the total level of glutamate associated with a particular astrocyte reaches the threshold F_{act}:

$$\frac{1}{N_a} \sum_{(i,j) \in N_a} \Theta(G^{(i,j)} - G_{thr}) > F_{act} \tag{10}$$

Here, we use $t_{glu} = 0.06$ s.

2.3. Astrocytic Network

Although voltage-gated calcium channels (VGCC) have been shown to be able to elevate intracellular calcium concentration and many authors included them in their mod-

els [68–71], here, we use the Ullah model [72] to simplify the description of the calcium dynamics within astrocytes where only the impact of glutamate is considered:

$$\begin{cases} \dfrac{dCa^{(m,n)}}{dt} = J_{ER}^{(m,n)} - J_{pump}^{(m,n)} + J_{leak}^{(m,n)} + J_{in}^{(m,n)} - J_{out}^{(m,n)} + diff_{Ca}^{(m,n)} \\ \dfrac{dh^{(m,n)}}{dt} = a_2 \left(d_2 \dfrac{IP_3^{(m,n)} + d_1}{IP_3^{(m,n)} + d_3} (1 - h^{(m,n)}) - Ca^{(m,n)} h^{(m,n)} \right) \end{cases} \tag{11}$$

The explicit forms of the individual terms are summarized as below:

$$\begin{cases} J_{ER} = c_1 v_1 Ca^3 h^3 IP_3^3 \dfrac{c_0/c_1 - (1 + 1/c_1)Ca}{(IP_3 + d_1)^3 (Ca + d_5)^3} \\ J_{pump} = \dfrac{v_3 Ca^2}{k_3^2 + Ca^2} \\ J_{leak} = c_1 v_2 (c_0/c_1 - (1 + 1/c_1)Ca) \\ J_{in} = \dfrac{v_6 IP_3^2}{k_2^2 + IP_3^2} \\ J_{out} = k_1 Ca \\ diff_{Ca} = d_{Ca}(\Delta Ca) \end{cases} \tag{12}$$

Here, Ca denotes the Ca^{2+} concentration within cytoplasm and h denotes the fraction of opened IP_3 receptors (IP3Rs) on the ER. We assume that the astrocytes are spatially homogeneous. ER is a continuous membrane system that stores a reservoir of Ca^{2+} within astrocytes. The released IP_3 then binds to IP3Rs on the ER and opens the channel allowing for the flow of Ca^{2+} from the ER into the cytoplasm, which is characterized by J_{ER}. In this model, we assume the co-existence of the ER and the cytoplasm in individual astrocytes and the homogeneous distribution of ER in the interior of astrocytes. J_{pump} denotes the ATP-dependent pump that recovers Ca^{2+} from the cytoplasm back to the ER. J_{leak} denotes the leakage of Ca^{2+} from the ER to the cytosol due to the concentration gradient. J_{in} and J_{out} denote the Ca^{2+} exchange with the extracellular space. $diff_{Ca}$ represents the diffusion of Ca^{2+} via gap junctions.

Finally, the calcium-dependent gliotransmitter-induced modulation of synaptic weight by the associated astrocyte via the N-methyl-D-asparate receptors (NMDARs) is defined as

$$\nu = \nu^{\star} \Theta(Ca - Ca_{thr}) \tag{13}$$

where $\nu^{\star}$ denotes the weight of the synapse as a result of the astrocytic modulation of synaptic transmission if the Ca^{2+} concentration is beyond the threshold required for gliotransmitter release, Ca_{thr}, and the fraction of spiking neurons associated with that astrocyte during the time interval τ_{syn} is above F_{astro}. The duration of feedback is denoted by τ_{astro} and we use $\tau_{astro} = 250$ ms.

2.4. Variation of Astrocytic Coverage

In order to study the working memory performance of the network under various astrocytic coverage areas, we need to vary the size of the astrocytic layer M. However, to ensure that each astrocyte modulates an identical size of neuronal square and there is no leftover neuron, the following equation must be satisfied:

$$\frac{W - 1}{l - p} = M \tag{14}$$

where p is the size of the overlapping edge. In this work, we fixed $p = 1$. Since the input image is of dimension 79×79, if $W = 79$, the equation is satisfied for $l = 2, 3, 4, 7$.

To analyze the effect of $l = 5, 6, 9$, the image is adjusted by adding a periphery of stripe of width 1 outside of the edge, the intensity of which is chosen to be the same as the background. Now $W = 81$ and the equation is satisfied. Similarly, the equation is satisfied for $l = 8$ by choosing $W = 78$ (edge removal on one side). In this way, the size of the image is by and large maintained and the digital patterns are least damaged.

2.5. Variation of Spatial Frequencies

In this work, we utilized low-pass filter to alter the spatial frequencies of the input image.

The 2D discrete forward Fourier transform converts the image from the spatial domain into the frequency domain with:

$$F(k,l) = \sum_{x=0}^{W-1} \sum_{y=0}^{W-1} f(x,y) e^{-i2\pi(\frac{kx}{W} + \frac{ly}{W})} \tag{15}$$

The inverse transform converts from the frequency domain back to the spatial domain with:

$$f(x,y) = \frac{1}{W^2} \sum_{k=0}^{W-1} \sum_{l=0}^{W-1} F(k,l) e^{i2\pi(\frac{kx}{W} + \frac{ly}{W})} \tag{16}$$

where $f(x,y)$ denotes the intensity at pixel (x,y) whilst $F(k,l)$ consists of the spectrum and the phase angle at frequency (k,l). In general, one is more concerned with the spectrum as compared to the angle so the angle is not within the scope of our discussion. Figure 2 displays what digit zero looks like in the spatial domain (left) and spectral domain (right), respectively. By convention, $F(0,0)$ is placed at the center of the spectral domain and is also the largest component of the image. Moreover, we display the frequency domain on the logarithmic scale so as to make the other frequency components more visible. The frequency increases as we move farther away from the center in the spectral domain.

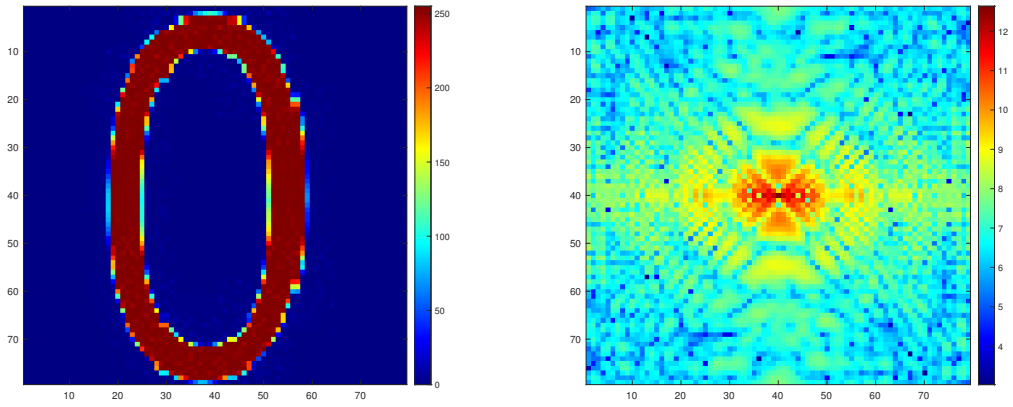

Figure 2. Spatial domain and spectral domain of digit 0.

A low-pass filter applies a threshold f_0 to the spectral domain and sets all the components above f_0 to zero. In this work, the filter will be applied to the input current at each time step. By slowly increasing the threshold, we hope to figure out the sensitivity of the short-term memory performance to the change in spatial frequencies.

2.6. Simulation Protocols

Most of the parameter values and protocols used in this work are identical to those in [35]. Since the size of our parameters is huge, we do not list the values used in this article. One can refer to [35] or https://github.com/zonglunli7515/Impact-of-astrocytic-coverage-of-synapses-and-spatial-frequencies-on-the-working-memory (accessed on 7 September 2022) for more details. Here, we only made a few adjustments in order to study the impact

of spatial frequencies in a more effective way. Therefore, unless otherwise specified, one can assume we herein use the same protocol as in [35].

The dynamics of the astrocytic network is simulated using the Runge-Kutta fourth-order method and the remaining part using the forward Euler method with time-step $\Delta t = 0.1$ ms. The input current I_{app} is converted from a digital image (0–9) with the same size of the neuronal network by scaling the pixel intensity, which will be used in the learning and the testing stage. The pixel intensity is scaled in the range $[0, A_{stim}]$ for learning and $[0, A_{test}]$ for testing in order to prevent over-excitation of neurons. In this work, we employ the binary encoding that converts intensity over 127 to A_{stim} (A_{test}) and to 0 otherwise. The input is also subject to salt-and-pepper noise which will also alter the frequency domain in addition to the low-pass filter. Different from a low-pass filter which will cut off the frequency components above a threshold, increasing the salt-and-pepper noise tends to include more frequency components (high frequency components in particular) as the noise will break the image down into pieces. We are interested in investigating the effect of both on the short-term memory performance. In this work, we do not introduce it in the learning stage to keep the real pattern intact and alter the noise level in the testing stage. Here, our work is only focused on the single-item implementation. This is to ensure that the real spatial pattern is fixed during the experiment. Unless otherwise specified, in the learning stage, the input current I_{app} is applied to the network at $t_1 = 0.1$ s for $t_{stim} = 200$ ms and in the testing stage, I_{app} is applied to the network at $t_2 = 2$ s for $t_{test} = 150$ ms. The simulation terminates at $t_e = 2.3$ s. We alter t_2 and t_e when investigating the impact of the time interval between training and testing. In addition, note that changing the frequency domain will result in complex values in the spatial domain when conducting the inverse transform. To this end, we take the absolute values and re-scale them with A_{stim} (A_{test}). Our simulation time is shorter as compared to the one used in [35] but the time interval between the learning and the testing stage is already long enough for the activation of calcium release within astrocytes.

2.7. Performance Measure

To measure the performance of our model, i.e., to what extent the model is able to memorize the real pattern, we came up with a correlation measure C_p that compares the recalled pattern (during testing) with the real pattern:

$$\begin{cases} M_{ij}(t) = I\left[\left(\sum\limits_{k=t}^{t+\omega} I[V_{ij}(k) > 30]\right) > thr\right] \\ CD(t) = \dfrac{1}{|P|}\sum\limits_{(i,j)\in P} M_{ij}(t) \\ CB(t) = \dfrac{1}{W^2 - |P|}\sum\limits_{(i,j)\notin P} (1 - M_{ij}(t)) \\ C(t) = \dfrac{1}{2}(CD(t) + CB(t)) \\ C_p = \max\limits_{thr} C(t) \end{cases} \tag{17}$$

Here t is the start time of the testing stage and we use $\omega = 250$ ms. P represents the set of pixels belonging to the real pattern. CD represents the true positive rate in our context, namely, how many pixels that belong to the real pattern have been recalled. Similarly, CB represents the true negative rate. Therefore, C can accurately reflect the overall performance of the neuron–astrocyte network. We select C_p that maximizes $C(t)$ over the whole-number thresholds, $thr = 1, 2, \ldots, 30$.

3. Results

In this chapter, we mainly show how short-term memory performance is affected by astrocytic coverage under various spatial frequencies and salt-and-pepper noise levels.

Figures 3 and 4 display the model's performance scores C_p for digit zero (a symmetric digit) and two (an asymmetric digit) under various conditions, respectively. Each square represents one single simulation using the protocol described in the last chapter. In each sub-figure, the vertical axis denotes various levels of the salt-and-pepper noise at the testing stage. The horizontal axis denotes the moving threshold f_0 (increased by 2 units) of the low-pass filter from $f_0 = 4$ to $f_0 = 58$. Namely, more frequencies will be included as we move farther away from the origin. The plot starting from $f_0 = 4$ is to ensure the visual contrast for the performance over $f_0 = 4$ and we explain in more detail why there exists a sharp rise in performance from 4 later. The filter threshold terminates at $f_0 = 58$ because it will already incorporate all frequency components with respect to the largest picture ($W = 81$) in this study.

On the one hand, for all sizes ($l = 2, 3, 4, 5, 6, 7, 8, 9$) of the astrocytic coverage and noise level during the testing stage, the performance plunges when moving the filter threshold from 5 to 4, which corresponds to $(5 \times 2)/79 \approx 1/8 - (4 \times 2)/79 \approx 1/10$ of the distance from the center to the edge in the spectral domain. On the other hand, the trace width of the digit in the image we use is about 8–10 pixels. By trace width we mean the interval between the boundaries of the digit. This makes it a wavelength of 16–20 (so a frequency of 1/16–1/20, namely 1/8–1/10 of the distance from the center to the edge in the frequency domain). This correspondence demonstrates that our short-term memory model does manage to detect the dominant frequency pattern of the input image. The performance of the other integer threshold (1,2,3) is not shown in Figures 3 and 4 because we would like to have a contrasting color scale for higher thresholds. As expected, the performance decreases sharply from $f_0 = 4$ to $f_0 = 0$ which is demonstrated in Figure 5. Here, the threshold is increased by 1 unit.

From Figures 3 and 4, we note that our model is mostly noise-tolerant up to the noise level equal to 0.1. This manifests that our network is able to precisely recall very analogous patterns but has some trouble recalling the exact patterns for less analogous inputs. Another notable feature is that there exists a shift in performance pattern under different filter thresholds as the astrocytic coverage size is increased from $l = 2$ to $l = 9$, which stands as the central observation of our research, and next, we use $l = 4$ and $l = 8$ to explain it at greater length.

From Figures 3 and 4, we observe that for $l = 4$, the performance color transitions from light red to dark and back to light at a relatively high noise level. Take for example noise level equal to 0.2 (Figure 6), a low filter threshold, $f_0 = 10$ smooths the picture and prevents over-firing of neurons. A high filter threshold, $f_0 = 58$, ensures that most of the digital pixels are firing, although at the cost of slight over-firing. However, a middle one, $f_0 = 40$ corrupts the picture to a certain degree and yields a relatively low performance. For $l = 8$, the performance color transitions from light red to dark and there exists a slight recovery before going dark again at high noise levels. At the noise level equal to 0.2 (Figure 7), the firing patterns of $f_0 = 10$ and $f_0 = 40$ are very similar to those in $l = 4$, despite the alteration in the astrocytic coverage. However, for $f_0 = 58$, $l = 8$ significantly favors the over-firing which results in many misclassifications, and $f_0 = 50$ is somewhere in the middle.

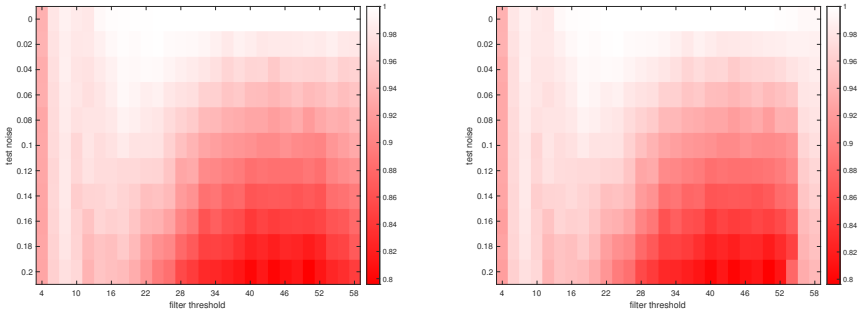

(a) $l = 2$ **(b)** $l = 3$

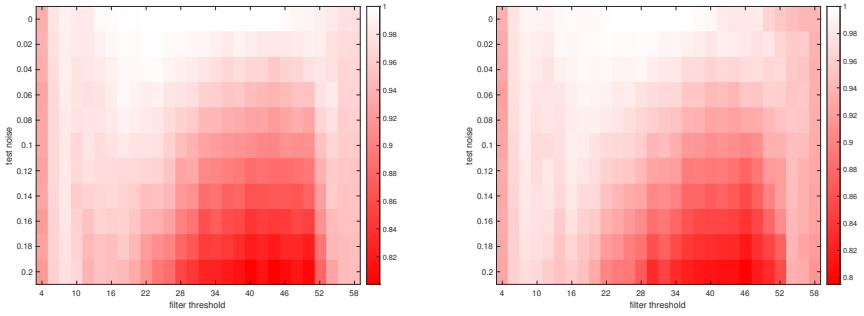

(c) $l = 4$ **(d)** $l = 5$

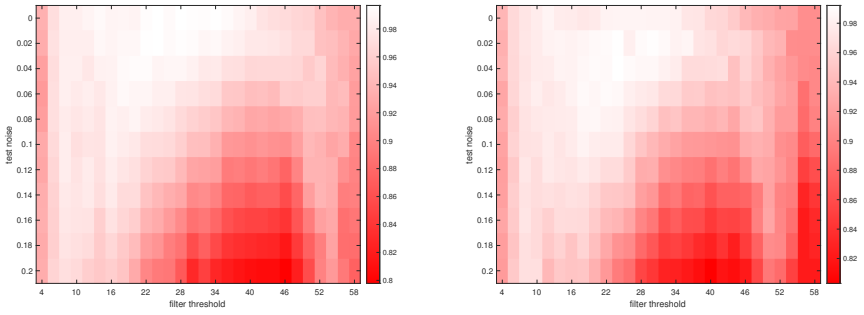

(e) $l = 6$ **(f)** $l = 7$

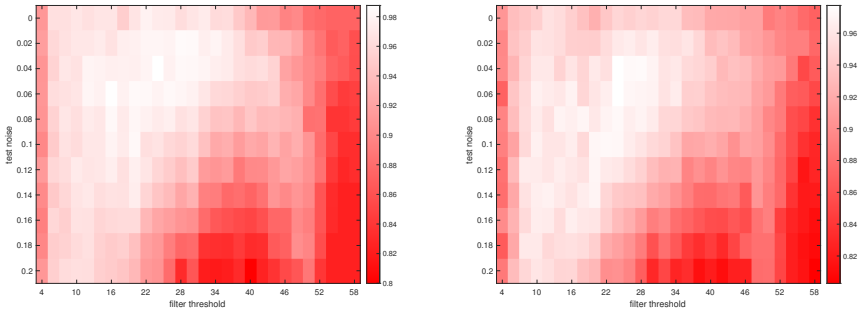

(g) $l = 8$ **(h)** $l = 9$

Figure 3. Performance score C_p for digit zero with various astrocytic coverage areas. In each subfigure, the vertical axis denotes various levels of the salt-and-pepper noise at the testing stage. The horizontal axis denotes the threshold f_0 (increased by 2 units) of the low-pass filter.

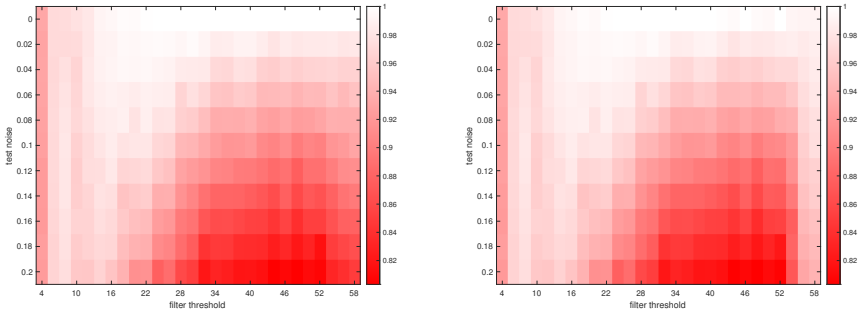

(a) $l = 2$

(b) $l = 3$

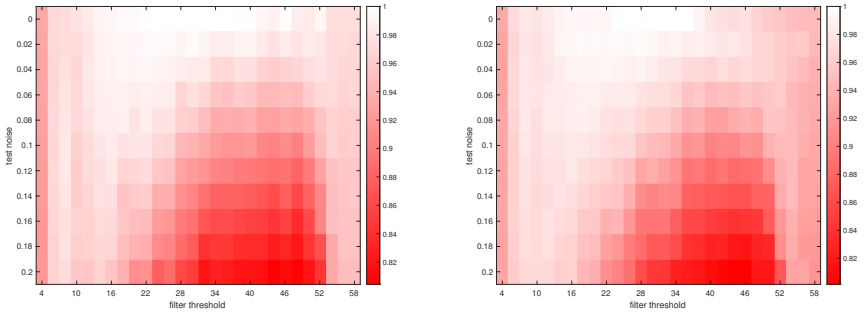

(c) $l = 4$

(d) $l = 5$

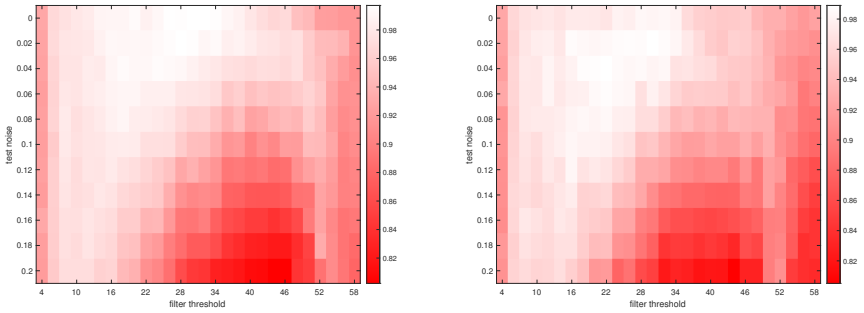

(e) $l = 6$

(f) $l = 7$

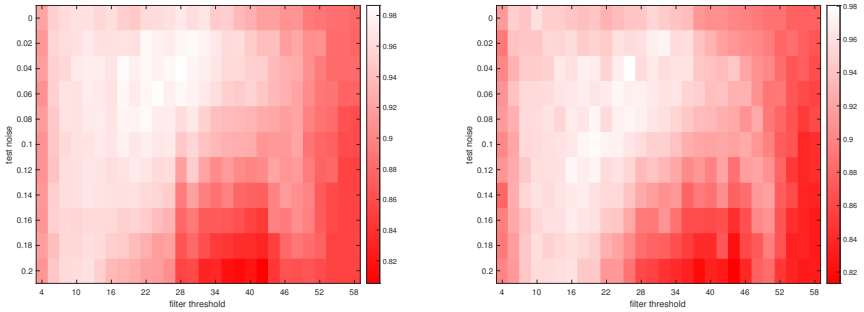

(g) $l = 8$

(h) $l = 9$

Figure 4. Performance score C_p for digit two with various astrocytic coverage areas. In each subfigure, the vertical axis denotes various levels of the salt-and-pepper noise at the testing stage. The horizontal axis denotes the threshold f_0 (increased by 2 units) of the low-pass filter.

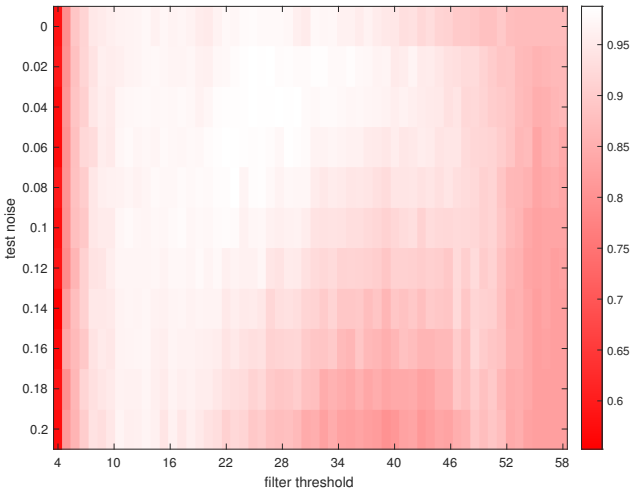

Figure 5. Performance score C_p at diverse levels of noise with $l = 8$ for digit zero including all the whole-number thresholds.

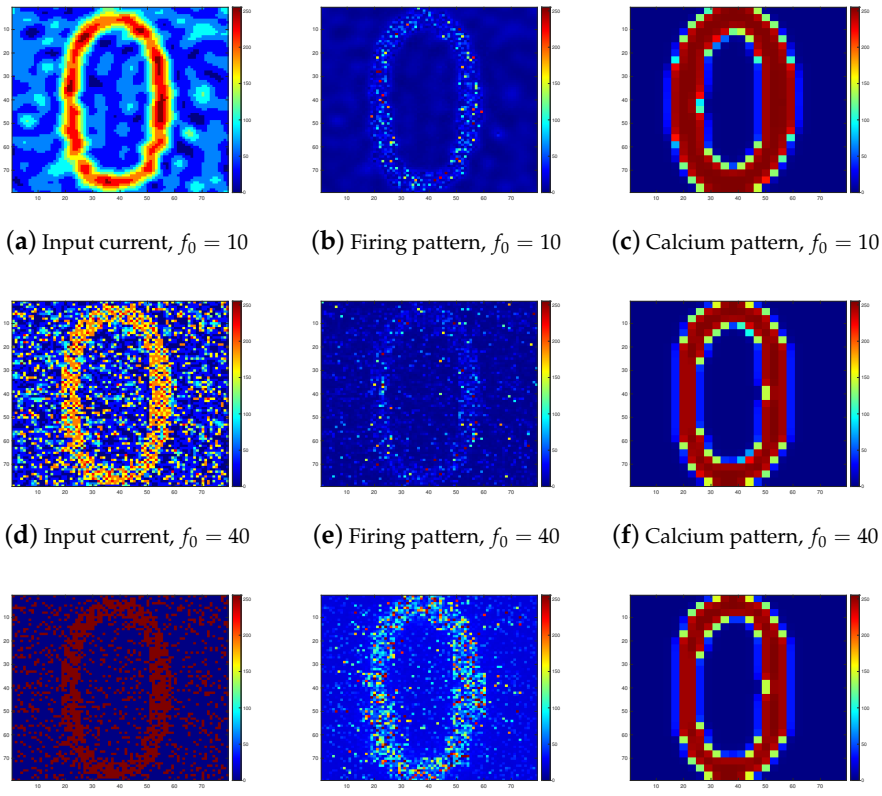

(a) Input current, $f_0 = 10$ **(b)** Firing pattern, $f_0 = 10$ **(c)** Calcium pattern, $f_0 = 10$

(d) Input current, $f_0 = 40$ **(e)** Firing pattern, $f_0 = 40$ **(f)** Calcium pattern, $f_0 = 40$

(g) Input current, $f_0 = 58$ **(h)** Firing pattern, $f_0 = 58$ **(i)** Calcium pattern, $f_0 = 58$

Figure 6. Snapshots for $l = 4$. The **left** panel displays the input current after being transformed by the low-pass filter at testing. The **middle** panel displays the firing pattern of neurons at $t = 2.1$ s. The **right** panel displays the calcium pattern of astrocytes at $t = 2$ s. In each sub-figure, the x- and y-axis denote the positional indices of the image. The colorbar describes the level of the input current, neuronal firing and astrocytic calcium concentration. The level has been scaled in the range 0–255 for visualization. The model exhibits very similar calcium patterns irrespective of the filter thresholds. From the first and the second column, we observe that $f_0 = 10$ smooths the picture and prevents over-firing of neurons; $f_0 = 58$ ensures that most of the digital pixels are firing; $f_0 = 40$ corrupts the picture to a certain degree. Therefore, the performance of $f_0 = 40$ is less desirable.

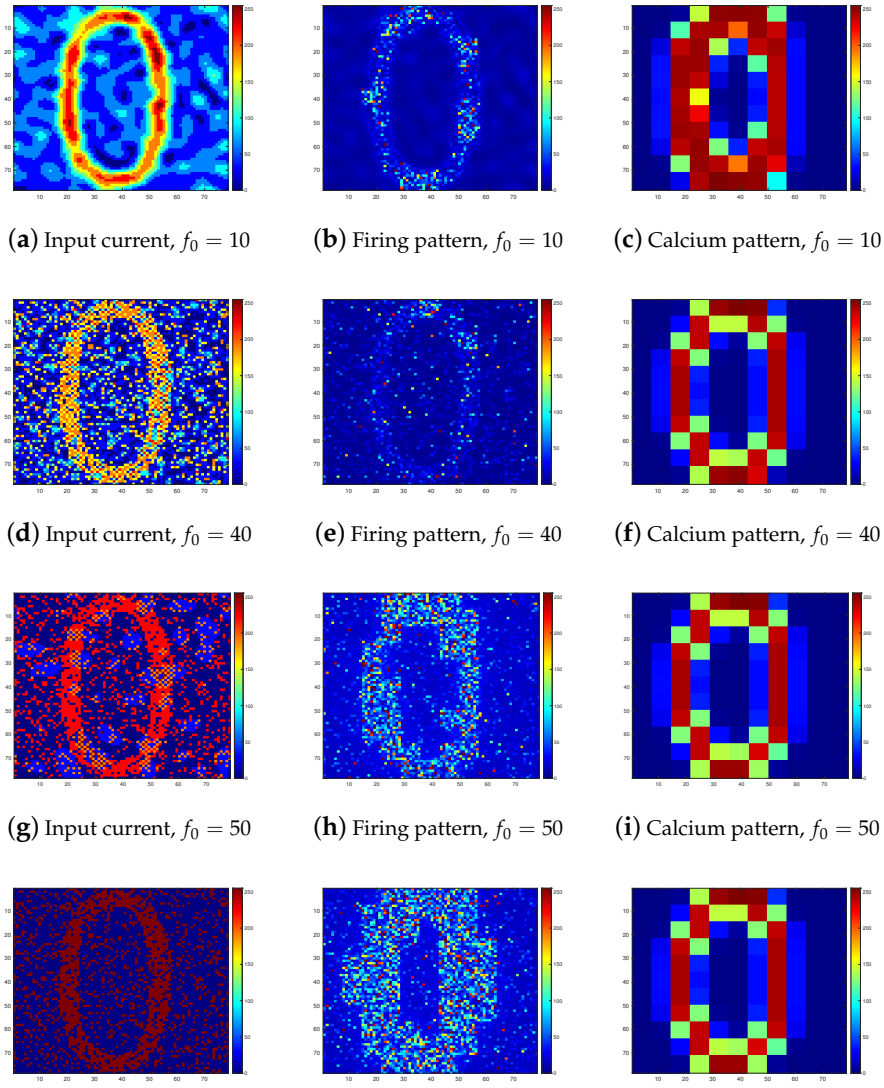

(a) Input current, $f_0 = 10$ **(b)** Firing pattern, $f_0 = 10$ **(c)** Calcium pattern, $f_0 = 10$

(d) Input current, $f_0 = 40$ **(e)** Firing pattern, $f_0 = 40$ **(f)** Calcium pattern, $f_0 = 40$

(g) Input current, $f_0 = 50$ **(h)** Firing pattern, $f_0 = 50$ **(i)** Calcium pattern, $f_0 = 50$

(j) Input current, $f_0 = 58$ **(k)** Firing pattern, $f_0 = 58$ **(l)** Calcium pattern, $f_0 = 58$

Figure 7. Snapshots for $l = 8$. The **left** panel displays the input current after being transformed by the low-pass filter at testing. The **middle** panel displays the firing pattern of neurons at $t = 2.1$ s. The **right** panel displays the calcium pattern of astrocytes at $t = 2$ s. In each sub-figure, the x- and y-axis denote the positional indices of the image. The colorbar describes the level of the input current, neuronal firing and astrocytic calcium concentration. The level has been scaled in the range 0–255 for visualization. The model exhibits very similar calcium patterns irrespective of the filter thresholds. From the first and the second column, we observe that $f_0 = 10$ smooths the picture and prevents over-firing of neurons; $f_0 = 40$ corrupts the picture to a certain degree; $f_0 = 58$ results in over-firing; $f_0 = 50$ is somewhere in the middle. Therefore, the performances of $f_0 = 40$ and $f_0 = 58$ are less desirable.

In order to better summarize the results shown in Figure 3, we use box plots to exhibit our statistical analysis. Figure 8a displays the overall short-term memory performance subject to low salt-and-pepper noises by grouping the noise level from 0 to 0.1. Similarly, the performance subject to high salt-and-pepper noises is shown in Figure 8b by grouping the noise level from 0.12 to 0.2. We note that at the low noise level, the overall performance starts to decrease at $l = 6$ and there does not exist a significant change in performance when it comes to the high noise, although $l = 4$ and $l = 5$ have a higher median. Figure 9a displays the overall short-term memory performance subject to low filter thresholds by

grouping the threshold from 4 to 22 and Figure 9b displays the performance subject to high filter thresholds by grouping the threshold from 24 to 58. In both of them, we have witnessed a slight decrease in performance from $l = 6$. The cutting points of 'low' and 'high' in the above cases are chosen based on the patterns shown in Figures 3 and 4. However, if we investigate the performance subject to individual filter thresholds, it could look very different from what is shown in Figure 9. For instance, in Figure 10, at $f_0 = 46$ the best median is achieved at $l = 7$ whilst at $f_0 = 18$ there is a decrease in performance after $l = 6$ which is similar to the overall result (Figure 9a). This may raise the possibility that different sizes of astrocytic coverage might optimize the performance at different spatial frequencies. However, we need to point out that the number of data at individual thresholds is limited and therefore, the difference may not be as considerable as shown in the figures.

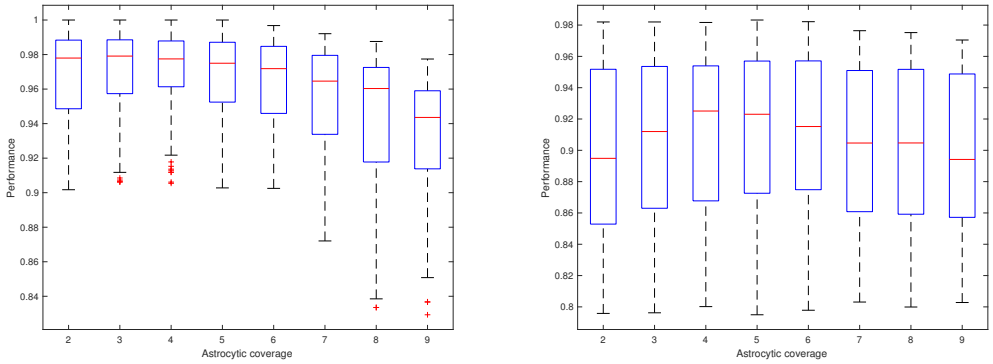

(**a**) Low noise (**b**) High noise

Figure 8. Short-term memory performance subject to low and high salt-and-pepper noises. The horizontal axis denotes the size of astrocytic coverage and the vertical axis denotes the performance score C_p. At the low noise level, the performance starts to decrease from $l = 6$; at the high noise level, there does not exist a significant change in performance, although the medians are slightly different.

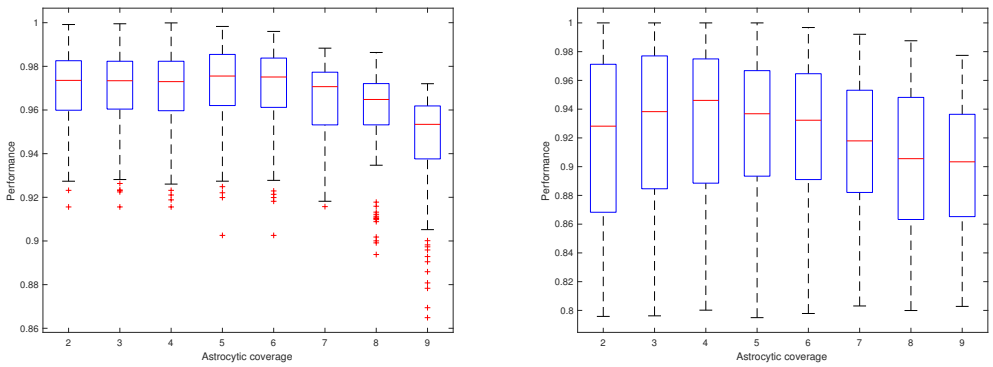

(**a**) Low-pass filter with low thresholds (**b**) Low-pass filter with high thresholds

Figure 9. Short-term memory performance subject to low-pass filter with low and high thresholds. The horizontal axis denotes the size of astrocytic coverage and the vertical axis denotes the performance score C_p. Both figures demonstrate a decline in performance from $l = 6$.

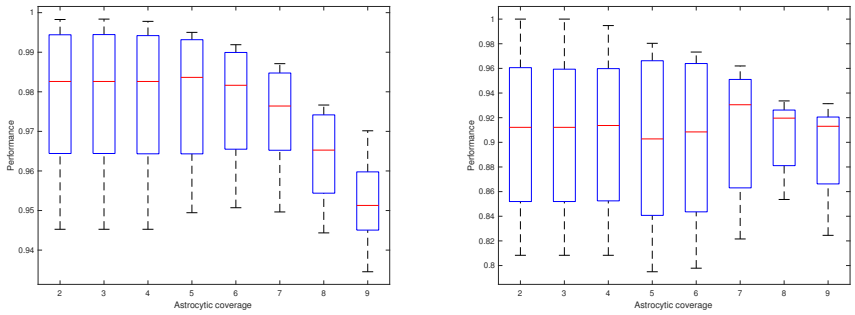

(**a**) $f_0 = 18$ (**b**) $f_0 = 46$

Figure 10. Short-term memory performance subject to two individual filter thresholds. The horizontal axis denotes the size of astrocytic coverage and the vertical axis denotes the performance score C_p. At individual thresholds, $f_0 = 18$ is similar to the overall performance of the low thresholds; the highest median of $f_0 = 46$ is achieved at $l = 7$.

We also observe that for a large astrocytic coverage, $l = 8$ for instance, a shorter time interval between training and testing tends to outperform a longer one when most of the frequency components have been included (Figure 11 right-end). Conversely, the performance barely changes with respect to a small astrocytic coverage such as $l = 4$ (Figure 12). For high filter thresholds, a longer time interval will result in more activated astrocytes as a result of calcium diffusion. However, a smaller astrocytic coverage has relatively little impact on the firing patterns of neurons at the testing stage because each astrocyte controls fewer neurons. Conversely, a bigger coverage will result in the over-firing of neurons in that more neurons that should not be activated have been activated, which decreases the performance. The above analysis is supported by the calcium patterns of astrocytes with different astrocytic coverage sizes and time intervals between training and testing shown in Figure 13. For relatively low filter thresholds, the firing pattern remains largely unchanged because of smoothing, as demonstrated previously.

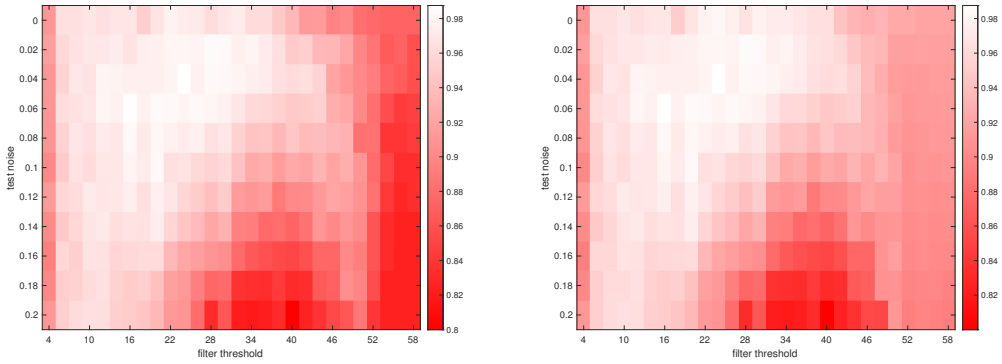

(**a**) $t_2 = 2$s, $t_e = 2.3$s (**b**) $t_2 = 1.5$s, $t_e = 1.8$s

Figure 11. The performance score C_p with different starting time t_2 with $l = 8$. In each sub-figure, the vertical axis denotes various levels of the salt-and-pepper noise at the testing stage. The horizontal axis denotes the threshold f_0 (increased by 2 units) of the low-pass filter. The right-end of (**a**) is darker than (**b**) and the remaining regions are nearly the same.

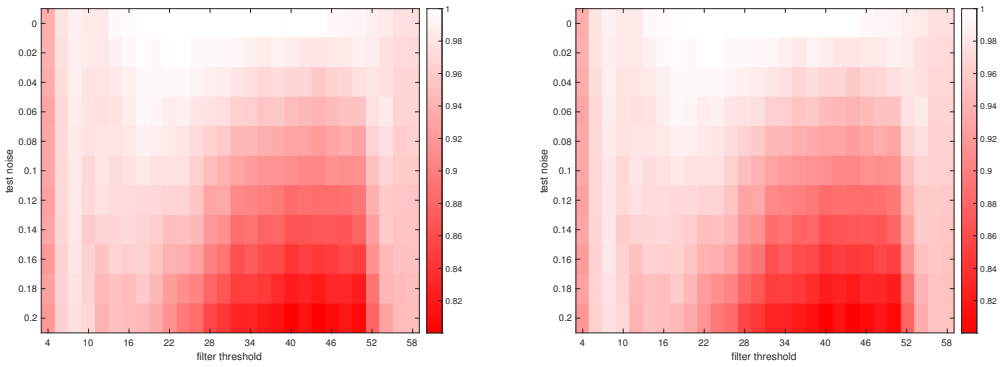

(**a**) $t_2 = 2$s, $t_e = 2.3$s (**b**) $t_2 = 1.5$s, $t_e = 1.8$s

Figure 12. The performance score C_p with different starting time t_2 with $l = 4$. In each sub-figure, the vertical axis denotes various levels of the salt-and-pepper noise at the testing stage. The horizontal axis denotes the threshold f_0 (increased by 2 units) of the low-pass filter. The performance is barely affected by the time interval.

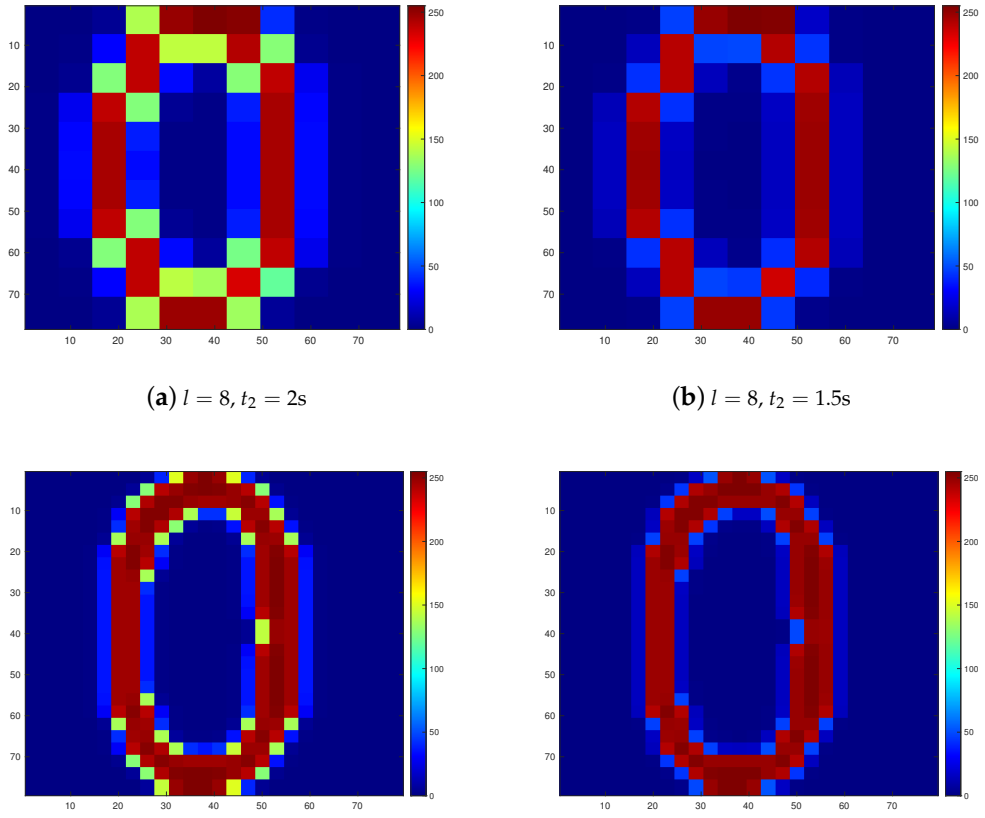

(**a**) $l = 8$, $t_2 = 2$s (**b**) $l = 8$, $t_2 = 1.5$s

(**c**) $l = 4$, $t_2 = 2$s (**d**) $l = 4$, $t_2 = 1.5$s

Figure 13. Calcium patterns of astrocytes with different astrocytic coverage areas and time intervals between training and testing. Here, we use $f_0 = 58$ and noise level equal to 0.2 as an example.

4. Discussions

In light of the results shown in Figures 3, 4, 9 and 10, there are two hypotheses that may sound plausible:

1. Astrocytes may adjust their coverage areas in response to the change in spatial frequencies in order to optimize the short-term memory.

2. Different astrocytes may have different coverage areas in order to process different frequency components in order to optimize the short-term memory.

To the best of our knowledge, these open questions have not been given enough consideration yet and therefore, our work aims to raise the awareness of these plausible relations so that interested researchers may test and verify them in laboratory. Hypothesis 1 and 2 are not identical but they are somehow similar and could co-exist. As shown in Figures 9 and 10, although the majority of $l = 4$ outperforms $l = 7$, at some specific thresholds ($f_0 = 46$ for instance) $l = 7$ gives a slightly better performance. This may raise an open question for experimentalists to validate whether astrocytes adjust their coverage areas in response to the changing spatial frequencies (hypothesis 1), or whether different astrocytes have different coverage areas (hypothesis 2), so as to assist the short-term memory. More precisely, it may be plausible to hypothesize that individual astrocytes are free to select from a wide range of coverage areas in order to optimally process the spatial information containing diverse frequency components; or at a particular time point, individual astrocytic modules, in which all astrocytes have identical coverage, process some particular frequency components and hierarchically summarize the information to achieve the optimal short-term memory. In all, one is interpreted from a dynamic viewpoint and the other one from a static viewpoint, but they do not contradict with each other. The former one may also help to explain the findings that the astrocytic coverage of synapses is highly dynamic. Additionally, over the last decade, emerging evidence has shown that astrocytes actively participate in the brain energy mechanisms and potentially assist the energy-efficient coding of neuronal circuits [73–75]. It is reasonable to reckon that a compactly connected astrocytic network tends to consume more energy, therefore it seems plausible that a sparse layout could become more favorable so long as the precision is not considerably compromised. The results may provide a new perspective for those who study the roles played by astrocytes in the cerebral energy-efficiency.

In regards to the small noise level, on the whole, a small astrocytic coverage tends to outperform a big one irrespective of the filter threshold. This may indirectly support the experimental result that the increasing density of astrocytes enhances short-term memory performances [47]. The comparison of $l = 2$, $l = 3$ and $l = 4$ also raises the potential to study whether over-crowded astrocytes will have negative effect on short-term memory for biologists.

As for the relatively high noise level, it appears that the performance score remains relatively low in a threshold interval and the more noisy the image is, the wider the interval is. We suppose the phenomenon is due to the fact that a higher salt-and-pepper noise distorts the original image more massively and the image decomposes into more frequency components (including many high frequencies). A relatively high filter threshold retains these frequencies (as a result of noise) which leads to a decrease in performance.

Finally, the sensitivity to the filter threshold also validates the necessity of introducing convolutional layers in spiking neural networks [76–78] for pattern recognition tasks because the idea of introducing filters is to extract the local patterns such as curves and straight lines.

One open question is whether the pattern displayed in Figure 3 will scale up with the size of the input image. Namely, when the size of the input is scaled up or down, whether the same pattern will be observed when the astrocytic coverage alters with the same ratio. This may shed light on the correspondence between the size of the input image and the astrocytic coverage.

To summarize, in this work, we leveraged a computational neuron–astrocyte model for short-term memory that has been recently developed to study the impact of astrocytic coverage and spatial frequencies on short-term memory. We demonstrated a shift in the performance of the short-term memory under different filter thresholds as the astrocytic coverage size is altered. We also raised two hypotheses about the potential relationship between astrocytic coverage, spatial frequencies and short-term memory. These hypothetical results emerged from several experimental facts which show that the rearrangement

of the structural interactions between synaptic elements and perisynaptic astrocytic processes alters the efficacy of neurotransmitter transport and gliotransmitter release, thereby inducing changes in the synaptic gain and long-term potentiation induction [79,80]. However, the role of astrocytic morphological plasticity in memory processes required further experimental evaluation including cellular and in vivo studies. In particular, different genetic-interference strategies which impact plasticity of structural interactions between astrocytes and synapses can be used to monitor memory impairments in animal studies [53]. We expect that the article can bring these unattended aspects to biologists' attention as a better understanding of this topic may pave the way for some transformative findings as to how neurons and glial cells adapt their behaviors in response to the external stimuli.

Author Contributions: Supervision: A.Z.; conceptualization: A.Z. and Z.L.; methods: S.G. and Z.L.; numerical simulation: Y.T. and Z.L.; writing: Z.L., A.Z., S.G. and Y.T. All authors have read and agreed to the published version of the manuscript.

Funding: This project was funded by Russian Science Foundation Grant No. 22-12-00216, UKRI Medical Research Council grant (MR/R02524X/1) and CRUK Early Detection Committee Project Award C12077/A26223.

Institutional Review Board Statement: Not applicable.

Informed Consent Statement: Not applicable.

Data Availability Statement: https://github.com/zonglunli7515/Impact-of-astrocytic-coverage-of-synapses-and-spatial-frequencies-on-the-working-memory (accessed on 7 September 2022).

Acknowledgments: Numerical simulations for this research was carried out in the frame of the scientific program of the National Center for Physics and Mathematics (project "Artificial intelligence and big data in technical, industrial, natural and social systems").

Conflicts of Interest: The authors declare no conflict of interest.

References

1. Latham, P.E.; Richmond, B.J.; Nelson, P.G.; Nirenberg, S. Intrinsic dynamics in neuronal networks. I. Theory. *J. Neurophysiol.* **2000**, *83*, 808–827. [CrossRef] [PubMed]
2. Van Pelt, J.; Vajda, I.; Wolters, P.S.; Corner, M.A.; Ramakers, G.J. Dynamics and plasticity in developing neuronal networks in vitro. *Prog. Brain Res.* **2005**, *147*, 171–188.
3. Roxin, A.; Montbrió, E. How effective delays shape oscillatory dynamics in neuronal networks. *Phys. Nonlinear Phenom.* **2011**, *240*, 323–345. [CrossRef]
4. Zhang, H.; Ye, M.; Ye, R.; Cao, J. Synchronization stability of Riemann–Liouville fractional delay-coupled complex neural networks. *Phys. Stat. Mech. Appl.* **2018**, *508*, 155–165. [CrossRef]
5. Michel, C.M.; Koenig, T. EEG microstates as a tool for studying the temporal dynamics of whole-brain neuronal networks: A review. *Neuroimage* **2018**, *180*, 577–593. [CrossRef]
6. Zhang, H.; Cheng, J.; Zhang, H.; Zhang, W.; Cao, J. Quasi-uniform synchronization of Caputo type fractional neural networks with leakage and discrete delays. *Chaos Solitons Fractals* **2021**, *152*, 111432. [CrossRef]
7. Zhang, H.; Cheng, Y.; Zhang, H.; Zhang, W.; Cao, J. Hybrid control design for Mittag-Leffler projective synchronization on FOQVNNs with multiple mixed delays and impulsive effects. *Math. Comput. Simul.* **2022**, *197*, 341–357. [CrossRef]
8. Agulhon, C.; Petravicz, J.; McMullen, A.B.; Sweger, E.J.; Minton, S.K.; Taves, S.R.; Casper, K.B.; Fiacco, T.A.; McCarthy, K.D. What is the role of astrocyte calcium in neurophysiology? *Neuron* **2008**, *59*, 932–946. [CrossRef]
9. Booth, H.D.; Hirst, W.D.; Wade-Martins, R. The role of astrocyte dysfunction in Parkinson's disease pathogenesis. *Trends Neurosci.* **2017**, *40*, 358–370. [CrossRef]
10. Upadhya, R.; Zingg, W.; Shetty, S.; Shetty, A.K. Astrocyte-derived extracellular vesicles: Neuroreparative properties and role in the pathogenesis of neurodegenerative disorders. *J. Control. Release* **2020**, *323*, 225–239. [CrossRef]
11. Rose, C.F.; Verkhratsky, A.; Parpura, V. Astrocyte glutamine synthetase: Pivotal in health and disease. *Biochem. Soc. Trans.* **2013**, *41*, 1518–1524. [CrossRef] [PubMed]
12. Brusilow, S.W.; Koehler, R.C.; Traystman, R.J.; Cooper, A.J. Astrocyte glutamine synthetase: Importance in hyperammonemic syndromes and potential target for therapy. *Neurotherapeutics* **2010**, *7*, 452–470. [CrossRef]
13. Gordleeva, S.; Kanakov, O.; Ivanchenko, M.; Zaikin, A.; Franceschi, C. Brain aging and garbage cleaning. *Semin. Immunopathol.* **2020**, *42*, 647–665. [CrossRef] [PubMed]
14. Haydon, P.G. GLIA: Listening and talking to the synapse. *Nat. Rev. Neurosci.* **2001**, *2*, 185–193. [CrossRef] [PubMed]

15. Parpura, V.; Haydon, P.G. Physiological astrocytic calcium levels stimulate glutamate release to modulate adjacent neurons. *Proc. Natl. Acad. Sci. USA* **2000**, *97*, 8629–8634. [CrossRef]
16. Araque, A.; Parpura, V.; Sanzgiri, R.P.; Haydon, P.G. Tripartite synapses: Glia, the unacknowledged partner. *Trends Neurosci.* **1999**, *22*, 208–215. [CrossRef]
17. Perea, G.; Araque, A. GLIA modulates synaptic transmission. *Brain Res. Rev.* **2010**, *63*, 93–102. [CrossRef]
18. Araque, A.; Parpura, V.; Sanzgiri, R.P.; Haydon, P.G. Glutamate-dependent astrocyte modulation of synaptic transmission between cultured hippocampal neurons. *Eur. J. Neurosci.* **1998**, *10*, 2129–2142. [CrossRef]
19. Halassa, M.M.; Fellin, T.; Haydon, P.G. The tripartite synapse: Roles for gliotransmission in health and disease. *Trends Mol. Med.* **2007**, *13*, 54–63. [CrossRef]
20. Santello, M.; Calì, C.; Bezzi, P. Gliotransmission and the tripartite synapse. *Synaptic Plast.* **2012**, 970, 307–331.
21. Volterra, A.; Magistretti, P.J.; Haydon, P.G. *The Tripartite Synapse: Glia in Synaptic Transmission*; Oxford University Press: Oxford, UK, 2002.
22. Perea, G.; Navarrete, M.; Araque, A. Tripartite synapses: Astrocytes process and control synaptic information. *Trends Neurosci.* **2009**, *32*, 421–431. [CrossRef] [PubMed]
23. Panatier, A.; Robitaille, R. Astrocytic mGluR5 and the tripartite synapse. *Neuroscience* **2016**, *323*, 29–34. [CrossRef] [PubMed]
24. Fellin, T.; Pascual, O.; Gobbo, S.; Pozzan, T.; Haydon, P.G.; Carmignoto, G. Neuronal synchrony mediated by astrocytic glutamate through activation of extrasynaptic NMDA receptors. *Neuron* **2004**, *43*, 729–743. [CrossRef] [PubMed]
25. Allegrini, P.; Fronzoni, L.; Pirino, D. The influence of the astrocyte field on neuronal dynamics and synchronization. *J. Biol. Phys.* **2009**, *35*, 413–423. [CrossRef]
26. Wade, J.J.; McDaid, L.J.; Harkin, J.; Crunelli, V.; Kelso, J.S. Bidirectional coupling between astrocytes and neurons mediates learning and dynamic coordination in the brain: A multiple modeling approach. *PLoS ONE* **2011**, *6*, e29445.
27. Chen, N.; Sugihara, H.; Sharma, J.; Perea, G.; Petravicz, J.; Le, C.; Sur, M. Nucleus basalis-enabled stimulus-specific plasticity in the visual cortex is mediated by astrocytes. *Proc. Natl. Acad. Sci. USA* **2012**, *109*, E2832–E2841. [CrossRef]
28. Gordleeva, S.Y.; Lebedev, S.A.; Rumyantseva, M.A.; Kazantsev, V.B. Astrocyte as a detector of synchronous events of a neural network. *JETP Lett.* **2018**, *107*, 440–445. [CrossRef]
29. Pankratova, E.V.; Kalyakulina, A.I.; Stasenko, S.V.; Gordleeva, S.Y.; Lazarevich, I.A.; Kazantsev, V.B. Neuronal synchronization enhanced by neuron–astrocyte interaction. *Nonlinear Dyn.* **2019**, *97*, 647–662. [CrossRef]
30. Gordleeva, S.Y.; Ermolaeva, A.V.; Kastalskiy, I.A.; Kazantsev, V.B. Astrocyte as spatiotemporal integrating detector of neuronal activity. *Front. Physiol.* **2019**, *10*, 294. [CrossRef]
31. Makovkin, S.Y.; Shkerin, I.V.; Gordleeva, S.Y.; Ivanchenko, M.V. Astrocyte-induced intermittent synchronization of neurons in a minimal network. *Chaos Solitons Fractals* **2020**, *138*, 109951. [CrossRef]
32. Makovkin, S.; Kozinov, E.; Ivanchenko, M.; Gordleeva, S. Controlling synchronization of gamma oscillations by astrocytic modulation in a model hippocampal neural network. *Sci. Rep.* **2022**, *12*, 6970. [CrossRef] [PubMed]
33. Gordleeva, S.; Tsybina, Y.A.; Krivonosov, M.I.; Tyukin, I.Y.; Kazantsev, V.B.; Zaikin, A.A.; Gorban, A.N. Situation-based memory in spiking neuron-astrocyte network. *arXiv* **2022**, arXiv:2202.07218.
34. Tsybina, Y.; Gordleeva, S.; Krivonosov, M.; Kastalskiy, I.; Zaikin, A.; Gorban, A. Modelling working memory in neuron-astrocyte network. In Proceedings of the 2021 International Joint Conference on Neural Networks (IJCNN) 2021, Shenzhen, China, 18–22 July 2021; pp. 1–6.
35. Gordleeva, S.Y.; Tsybina, Y.A.; Krivonosov, M.I.; Ivanchenko, M.V.; Zaikin, A.A.; Kazantsev, V.B.; Gorban, A.N. Modelling working memory in spiking neuron network accompanied by astrocytes. *Front. Cell. Neurosci.* **2021**, *15*, 86. [CrossRef] [PubMed]
36. Tsybina, Y.; Kastalskiy, I.; Krivonosov, M.; Zaikin, A.; Kazantsev, V.; Gorban, A.; Gordleeva, S. Astrocytes mediate analogous memory in a multi-layer neuron-astrocytic network. *Neural Comput. Appl.* **2022**, *34*, 9147–9160. [CrossRef]
37. Tsybina, Y.; Krivonosov, M.; Gordleeva, S.; Zaikin, A.; Gorban, A. Short-term memory in neuron-astrocyte network. In Proceedings of the 2020 4th Scientific School on Dynamics of Complex Networks and Their Application in Intellectual Robotics (DCNAIR), Innopolis, Russia, 9–11 September 2020; pp. 245–247.
38. Kastalskiy, I.; Tsybina, Y.; Kazantsev, V.; Gordleeva, S. Astrocytes' signals guided storage and retrieval of patterns by an SNN. In Proceedings of the 2021 Third International Conference Neurotechnologies and Neurointerfaces (CNN), Kaliningrad, Russia, 13–15 September 2021; pp. 34–37.
39. Abrego, L.; Gordleeva, S.; Kanakov, O.; Krivonosov, M.; Zaikin, A. Estimating integrated information in bidirectional neuron-astrocyte communication. *Phys. Rev. E* **2021**, *103*, 022410. [CrossRef] [PubMed]
40. Kanakov, O.; Gordleeva, S.; Ermolaeva, A.; Jalan, S.; Zaikin, A. Astrocyte-induced positive integrated information in neuron-astrocyte ensembles. *Phys. Rev. E* **2019**, *99*, 012418. [CrossRef]
41. Abrego Rangel, L.A. Information Processing in Biological Complex Systems: A View to Bacterial and Neural Complexity. Ph.D. Thesis, UCL (University College London), London, UK, 2021.
42. Kanakov, O.; Gordleeva, S.; Zaikin, A. Integrated Information in the Spiking–Bursting Stochastic Model. *Entropy* **2020**, *22*, 1334. [CrossRef]
43. Suzuki, A.; Stern, S.A.; Bozdagi, O.; Huntley, G.W.; Walker, R.H.; Magistretti, P.J.; Alberini, C.M. Astrocyte-neuron lactate transport is required for long-term memory formation. *Cell* **2011**, *144*, 810–823. [CrossRef]

44. Habbas, S.; Santello, M.; Becker, D.; Stubbe, H.; Zappia, G.; Liaudet, N.; Klaus, F.R.; Kollias, G.; Fontana, A.; Pryce, C.R.; et al. Neuroinflammatory TNFα impairs memory via astrocyte signaling. *Cell* **2015**, *163*, 1730–1741. [CrossRef]
45. Adamsky, A.; Kol, A.; Kreisel, T.; Doron, A.; Ozeri-Engelhard, N.; Melcer, T.; Refaeli, R.; Horn, H.; Regev, L.; Groysman, M.; et al. Astrocytic activation generates de novo neuronal potentiation and memory enhancement. *Cell* **2018**, *174*, 59–71. [CrossRef]
46. Kozachkov, L.; Michmizos, K.P. Sequence Learning in Associative Neuronal-Astrocytic Networks. In Proceedings of the International Conference on Brain Informatics, Padua, Italy, 19 September 2020; Springer: Cham, Switzerland, 2020; pp. 349–360.
47. De Luca, S.N.; Soch, A.; Sominsky, L.; Nguyen, T.X.; Bosakhar, A.; Spencer, S.J. Glial remodeling enhances short-term memory performance in Wistar rats. *J. Neuroinflamm.* **2020**, *17*, 1–8. [CrossRef] [PubMed]
48. Cowan, N. Working memory underpins cognitive development, learning, and education. *Educ. Psychol. Rev.* **2014**, *26*, 197–223. [CrossRef] [PubMed]
49. Baddeley, A. Working memory: The interface between memory and cognition. *J. Cogn. Neurosci.* **1992**, *4*, 281–288. [CrossRef]
50. Nairne, J.S. Short-term/working memory. In *Memory 1 January 1996*; Academic Press: Cambridge, MA, USA, 1996; pp. 349–360.
51. Lima, A.; Sardinha, V.M.; Oliveira, A.F.; Reis, M.; Mota, C.; Silva, M.A.; Marques, F.; Cerqueira, J.J.; Pinto, L.; Sousa, N.; et al. Astrocyte pathology in the prefrontal cortex impairs the cognitive function of rats. *Mol. Psychiatry* **2014**, *19*, 834–841. [CrossRef] [PubMed]
52. Robin, L.M.; da Cruz, J.F.; Langlais, V.C.; Martin-Fernez, M.; Metna-Laurent, M.; Busquets-Garcia, A.; Bellocchio, L.; Soria-Gomez, E.; Papouin, T.; Varilh, M.; et al. Astroglial CB1 receptors determine synaptic D-serine availability to enable recognition memory. *Neuron* **2018**, *98*, 935–944. [CrossRef] [PubMed]
53. Santello, M.; Toni, N.; Volterra, A. Astrocyte function from information processing to cognition and cognitive impairment. *Nat. Neurosci.* **2019**, *22*, 154–166. [CrossRef]
54. Akther, S.; Hirase, H. Assessment of astrocytes as a mediator of memory and learning in rodents. *Glia* **2021**, *70*, 1484–1505. [CrossRef]
55. Chung, W.S.; Allen, N.J.; Eroglu, C. Astrocytes control synapse formation, function, and elimination. *Cold Spring Harb. Perspect. Biol.* **2015**, *7*, a020370. [CrossRef]
56. Heller, J.P.; Rusakov, D.A. Morphological plasticity of astroglia: Understanding synaptic microenvironment. *Glia* **2015**, *63*, 2133–2151. [CrossRef]
57. Rusakov, D.A. Disentangling calcium-driven astrocyte physiology. *Nat. Rev. Neurosci.* **2015**, *16*, 226–233. [CrossRef]
58. Tanaka, M.; Shih, P.Y.; Gomi, H.; Yoshida, T.; Nakai, J.; Ando, R.; Furuichi, T.; Mikoshiba, K.; Semyanov, A.; Itohara, S. Astrocytic Ca^{2+} signals are required for the functional integrity of tripartite synapses. *Mol. Brain* **2013**, *6*, 1–3. [CrossRef] [PubMed]
59. Wu, Y.W.; Tang, X.; Arizono, M.; Bannai, H.; Shih, P.Y.; Dembitskaya, Y.; Kazantsev, V.; Tanaka, M.; Itohara, S.; Mikoshiba, K.; et al. Spatiotemporal calcium dynamics in single astrocytes and its modulation by neuronal activity. *Cell Calcium* **2014**, *55*, 119–129. [CrossRef] [PubMed]
60. Kustikova, V.; Krivonosov, M.; Pimashkin, A.; Denisov, P.; Zaikin, A.; Ivanchenko, M.; Meyerov, I.; Semyanov, A. CalciumCV: Computer vision software for calcium signaling in astrocytes. In Proceedings of the International Conference on Analysis of Images, Social Networks and Texts, Moscow, Russia, 5 July 2018; Springer: Cham, Switzerland, 2018; pp. 168–179.
61. Matrosov, V.; Gordleeva, S.; Boldyreva, N.; Ben-Jacob, E.; Kazantsev, V.; Pittà, M.D. Emergence of regular and complex calcium oscillations by inositol 1, 4, 5-trisphosphate signaling in astrocytes. In *Springer Series in Computational Neuroscience*; Springer International Publishing: Berlin/Heidelberg, Germany, 2019; pp. 151–176.
62. Izhikevich, E.M. Simple model of spiking neurons. *IEEE Trans. Neural Netw.* **2003**, *14*, 1569–1572. [CrossRef]
63. Kazantsev, V.B.; Asatryan, S.Y. Bistability induces episodic spike communication by inhibitory neurons in neuronal networks. *Phys. Rev. E* **2011**, *84*, 031913. [CrossRef]
64. Kazantsev, V.; Gordleeva, S.; Stasenko, S.; Dityatev, A. A homeostatic model of neuronal fring governed by feedback signals from the extracellular matrix. *PLoS ONE* **2012**, *7*, e41646. [CrossRef]
65. Gordleeva, S.Y.; Stasenko, S.V.; Semyanov, A.V.; Dityatev, A.E.; Kazantsev, V.B. Bi-directional astrocytic regulation of neuronal activity within a network. *Front. Comput. Neurosci.* **2012**, *6*, 92. [CrossRef] [PubMed]
66. Berridge, M.J. The inositol trisphosphate/calcium signaling pathway in health and disease. *Physiol. Rev.* **2016**, *96*, 1261–1296. [CrossRef]
67. Berridge, M.J. Inositol trisphosphate and calcium signalling. *Nature* **1993**, *361*, 315–325. [CrossRef] [PubMed]
68. Nadkarni, S.; Jung, P. Modeling synaptic transmission of the tripartite synapse. *Phys. Biol.* **2007**, *4*, 1. [CrossRef]
69. Oschmann, F.; Berry, H.; Obermayer, K.; Lenk, K. From in silico astrocyte cell models to neuron-astrocyte network models: A review. *Brain Res. Bull.* **2018**, *136*, 76–84. [CrossRef]
70. Liu, L.; Gao, H.; Zaikin, A.; Chen, S. Unraveling Aβ-mediated multi-pathway calcium dynamics in astrocytes: Implications for Alzheimer's Disease treatment from simulations. *Front. Physiol.* **2021**, *12*, 767892. [CrossRef] [PubMed]
71. Wu, Y.W.; Gordleeva, S.; Tang, X.; Shih, P.Y.; Dembitskaya, Y.; Semyanov, A. Morphological profile determines the frequency of spontaneous calcium events in astrocytic processes. *Glia* **2019**, *67*, 246–262. [CrossRef] [PubMed]
72. Ullah, G.; Jung, P.; Cornell-Bell, A.H. Anti-phase calcium oscillations in astrocytes via inositol (1, 4, 5)-trisphosphate regeneration. *Cell Calcium* **2006**, *39*, 197–208. [CrossRef] [PubMed]
73. Belanger, M.; Allaman, I.; Magistretti, P.J. Brain energy metabolism: Focus on astrocyte-neuron metabolic cooperation. *Cell Metab.* **2011**, *14*, 724–738. [CrossRef]

74. Stobart, J.L.; Anderson, C.M. Multifunctional role of astrocytes as gatekeepers of neuronal energy supply. *Front. Cell. Neurosci.* **2013**, *7*, 38. [CrossRef]
75. Kastanenka, K.V.; Moreno-Bote, R.; De Pittà, M.; Perea, G.; Eraso-Pichot, A.; Masgrau, R.; Poskanzer, K.E.; Galea, E. A roadmap to integrate astrocytes into Systems Neuroscience. *Glia* **2020**, *68*, 5–26. [CrossRef]
76. Tavanaei, A.; Maida, A.S. Multi-layer unsupervised learning in a spiking convolutional neural network. In Proceedings of the 2017 International Joint Conference on Neural Networks (IJCNN), Anchorage, AK, USA, 14–19 May 2017 ; pp. 2023–2030.
77. Lee, C.; Srinivasan, G.; Panda, P.; Roy, K. Deep spiking convolutional neural network trained with unsupervised spike-timing-dependent plasticity. *IEEE Trans. Cogn. Dev. Syst.* **2018**, *11*, 384–394.
78. Tavanaei, A.; Ghodrati, M.; Kheradpisheh, S.R.; Masquelier, T.; Maida, A. Deep learning in spiking neural networks. *Neural Netw.* **2019**, *111*, 47–63. [CrossRef]
79. Panatier, A.; Theodosis, D.T.; Mothet, J.P.; Touquet, B.; Pollegioni, L.; Poulain, D.A.; Oliet, S.H. Glia-derived D-serine controls NMDA receptor activity and synaptic memory. *Cell* **2006**, *125*, 775–784. [CrossRef]
80. Pannasch, U.; Freche, D.; Dallérac, G.; Ghézali, G.; Escartin, C.; Ezan, P.; Cohen-Salmon, M.; Benchenane, K.; Abudara, V.; Dufour, A.; et al. Connexin 30 sets synaptic strength by controlling astroglial synapse invasion. *Nat. Neurosci.* **2014**, *17*, 549–558. [CrossRef]